

Ground state properties of the one dimensional Coulomb gas.

Michele Casula,¹ Sandro Sorella,^{2,3} and Gaetano Senatore^{2,4}

¹ *Department of Physics, University of Illinois at Urbana-Champaign, 1110 W. Green St, Urbana, IL 61801, USA*

² *INFN Democritos National Simulation Center, Trieste, Italy*

³ *International School for Advanced Studies (SISSA) Via Beirut 2,4 34014 Trieste, Italy*

⁴ *Dipartimento di Fisica Teorica dell' Università di Trieste, Strada Costiera 11, 34014 Trieste, Italy*

(Dated: March 30, 2018)

We study the ground state properties of a quasi one dimensional electron gas, interacting via an effective potential with a harmonic transversal confinement and long range Coulomb tail. The exact correlation energy has been calculated for a wide range of electron densities by using the lattice regularized diffusion Monte Carlo method, which is a recent development of the standard projection Monte Carlo technique. In this case it is particularly useful as it allows to sample the exact ground state of the system, even in the low density regime when the exchange between electrons is extremely small. For different values of the width parameter b ($0.1 a_0^* \leq b \leq 4 a_0^*$), we give a simple parametrization of the correlation energy, which provides an accurate local density energy functional for quasi one dimensional systems. Moreover we show that static correlations are in qualitative agreement with those obtained for the Luttinger liquid model with long range interactions.

I. INTRODUCTION

The recent experimental realizations of ideally clean quasi one dimensional (Q1D) systems, like ultra cold Fermi gases in elongated harmonic traps¹ and high mobility quantum wires in the so-called cleaved edge overgrowth samples², have stimulated a new intense theoretical effort to explain the physical outcome of these systems. The low dimensionality brings about peculiar phenomena such as the fractionalized (0.7 structure) conductance^{3,4}, enhances the effect of localization (Wigner crystallization)^{4,5}, breaks the validity of the Fermi-liquid paradigm, which must be abandoned in favor of the Tomonaga-Luttinger liquid (TLL) concept⁶. One of the most striking consequences of the Luttinger theory is the spin-charge separation, which has been seen in a series of remarkable experiments carried out by Auslaender *et al.*, who were able to resolve the dispersion energy of elementary spin and charge excitations^{4,7}. They used the tunneling current between two parallel wires to probe the properties within one of the two wires. However, their measurements exhibit some features, like fringes in the tunneling pattern and non unitary conductance, that are not completely understood.

The finite-size effects, the disorder and the inhomogeneity of the device can play a crucial role to quantitatively explain the experiments^{8,9,10}. In this paper we will rather focus on the simpler homogeneous Q1D electron gas with harmonic transversal confinement and effective interactions with a long range Coulomb tail ($1/r$). The details of the confinement only affect the behavior at short range of the effective potential, and many models^{11,12,13,14,15} have been proposed which give an equivalent description of the homogeneous Q1D Coulomb gas. Despite its simplicity and a huge amount of theoretical work^{16,17,18,19,20} done to understand its properties, an accurate parametrization of its correlation energy is still missing. Indeed, the calculation of the ground state

energy of 1D wires with realistic Coulomb interactions is still an open problem, since the TLL is an effective low energy theory, and the RPA perturbative expansion is correct only in the high density limit. Recently a mapping of the problem with realistic Coulomb interaction onto exactly solvable models has been proposed²¹, but within this scheme several approximations are required for different density regimes. Previously an STLS-like²³ method was used by Calmels and Gold^{22,24} to compute the correlation energy, but it turns out to be not accurate enough to yield the correct ground state in the low density regime. Indeed, it predicts a Bloch instability ruled out by the Lieb-Mattis theorem²⁵.

Projection quantum Monte Carlo (QMC) techniques are exact in one dimension, since in this case the ground state (GS) nodes are known exactly²⁶, and the so called fixed node approximation, which cures the well known sign problem, does not affect the results. However, previous diffusion Monte Carlo (DMC) simulations²⁷ suffered from a lack of ergodicity at low electron densities, when the exchange between electrons become exponentially small. Other QMC attempts²⁸ to study the Q1D electron gas used the “world-line” algorithm on the lattice after a naive discretization of the Laplacian. Here we apply the novel lattice regularized diffusion Monte Carlo (LRDMC)²⁹, which is more efficient than previous projection QMC methods at low density, where it substantially alleviates the lack of exchanges between electrons.

The aim of this work is to provide a simple and efficient parametrization of the ground state correlation energy, exactly computed for the unpolarized system. Other ground state properties are also studied, like the spin and charge structure factors, which reveal a strong similarity with those computed using a TLL with long range interactions¹⁶. Therefore our parametrization can be an extremely useful input of density functional theory (DFT) calculations of Q1D systems with local density approximation (LDA), which can include the homoge-

neous Q1D electron gas with realistic long range interactions and TLL features as the reference system. Previous successful attempts have been limited so far to model systems such as the Luttinger liquid³⁰ or the one dimensional Hubbard model³¹, that have been successfully used as the reference systems for DFT simulations of Q1D ultra cold inhomogeneous atomic gases. We believe that an essentially exact calculation of the correlation energy, presented in this paper, should open the way for a wide range of relevant realistic applications in the field of Q1D systems.

The paper is organized as follows. In Chap. II we present the model for the Q1D homogeneous electron gas, in Chap. III we describe the variational ansatz used in our simulations, in Chap. IV we briefly review the LRDMC method and we compare it with the standard DMC algorithm. The results are reported in Chap. V, where we present the parametrization of the correlation energy with different values of the transversal confinement, and in Chap. VI, where we study the charge and spin structure factors. Finally, the conclusions are drawn in Chap. VII. In the end, two appendices explain how to compute the RPA correlation energy at high densities, and how to estimate the plasmon excitations from the knowledge of the static structure factor.

II. MODEL

In this paper we study a realistic model for a quantum wire with the lateral confinement provided by a harmonic transversal potential $V(r_{\perp}) = \frac{r_{\perp}^2}{4b^4}$, where b tunes the strength of the confinement and measures the wire width. Here and henceforth we use the effective Bohr radius $a_0^* = \frac{\hbar^2 \epsilon}{m^* e^2}$ as length unit and the effective Rydberg $Ryd^* = \frac{e^2}{2\epsilon a_0^*}$ as energy unit, where ϵ is the dielectric constant of the semiconducting medium and m^* is the effective mass of the electrons in the semiconductor. The electrons in the wire interact via a long range Coulomb potential. If the confinement is sufficiently strong, the ground state (GS) of this system can be approximated with good accuracy by a wave function with longitudinal and transversal components factorized. In particular we neglect any contribution from higher subbands of the lateral direction and we take the GS of the two dimensional harmonic oscillator as the transversal part of the total wave function. This approximation is valid whenever

$$r_s \gg \frac{\pi b}{4}, \quad (1)$$

where r_s is the Wigner-Seitz radius ($2r_s = 1/\rho$ is the mean interparticle distance), i.e. for sufficiently low electronic density.

Tracing out the transverse motion from the full Schrödinger equation by integration over the lateral coordinates of the particles yields¹¹, for N particle on a segment of length L , the one dimensional (1D) Hamiltonian

$$H = - \sum_{i=1}^N \nabla_i^2 + \frac{1}{2L} \sum_{k \neq 0} \tilde{V}_b(k) [\rho(k)\rho(-k) - N] \quad (2)$$

with $\rho(k) = \sum_j \exp(ikx_j)$ the Fourier transform of the one-body density operator and

$$\tilde{V}_b(k) = 2E_1(b^2 k^2) \exp(b^2 k^2). \quad (3)$$

Above E_1 is the exponential integral function and in Eq. (2) a suitable rigid positive charge background exactly cancels the $k = 0$ term. The real space 1D interparticle potential,

$$V_b(x) = \frac{\sqrt{\pi}}{b} \exp\left(\frac{x^2}{4b^2}\right) \operatorname{erfc}\left(\frac{|x|}{2b}\right), \quad (4)$$

has a long-range Coulomb tail but is finite at the origin.

Since in this work we focus on the GS properties of the wire, we work in the sector of vanishing total spin component along the z quantization axis, namely $N^{\uparrow} = N^{\downarrow} = N/2$. Obviously this choice is not a restriction because the ground state certainly belongs to this sector, regardless of its total spin. On the other hand the value of the total spin is known from the Lieb-Mattis theorem and Ref. 27: the GS of the one dimensional Coulomb gas is always a singlet for *all* densities. In order to perform a finite-size scaling analysis of the energy and correlation functions, we carried out QMC simulations with different number of particles, going from $N = 10$ to $N = 162$ and with an odd number of particles per each spin so that the degeneracy effects are avoided. With the aim to further reduce the finite-size bias, we considered the Hamiltonian in Eq. 2 with periodic boundary conditions (PBC) and with an infinite number of replicas of the simulation box (supercell). Thus, an electron in a supercell interacts with the other electrons in the supercell, their images, its own images, and the background. It is then convenient to define an effective interparticle potential, by summing the bare interaction of a particle and its background with a second particle over all its images, to obtain a periodic function:

$$\begin{aligned} V(x) &= \sum_n \left[V_b(x + nL) - \frac{1}{L} \int_{-L/2}^{L/2} dy V_b(x + nL - y) \right] \\ &= \frac{1}{L} \sum_{n \neq 0} \tilde{V}_b(G_n) e^{iG_n x}. \end{aligned} \quad (5)$$

In the above expression L is the length of the simulation box, n takes relative integer values and $G_n = 2\pi n/L$ is a reciprocal vector of the 1D Bravais lattice with primitive unit cell of length L . Since V_b is a long-range potential, we resort to an Ewald-like method³² to compute the sum in Eq. 5. The short-range part of the potential V and its long-range tail are treated in a different fashion, the former being summed in the direct space, the latter in the reciprocal one. The Ewald's procedure yields:

$$V(x) = V_{\text{sr}}(x) + V_{\text{lr}}(x), \quad (6)$$

$$V_{\text{sr}}(x) = \frac{\sqrt{\pi}}{b} \sum_{n=-\infty}^{+\infty} \exp\left[(x - nL)^2 / 4b^2\right] \operatorname{erfc}\left(\frac{|x - nL|}{2b}\right) - \sum_{n=-\infty}^{+\infty} \frac{2}{|x - nL|} \operatorname{erf}\left(\frac{|x - nL|}{2b}\right), \quad (7)$$

$$V_{\text{lr}}(x) = 2 \sum_{n>0} \frac{\cos(G_n x)}{L} e^{-(bG_n)^2} \tilde{V}_b(G_n). \quad (8)$$

In practice, we have worked with the Hamiltonian

$$H = - \sum_{i=1}^N \nabla_i^2 + \sum_{i<j} V(x_{ij}) + \frac{N}{2} V_{\text{MAD}}, \quad (9)$$

where $V_{\text{MAD}} = V(0) - V_b(0)$ is the Madelung energy, i.e., the interaction of a particle with its own images. We have used a tabulation for the potential $V(x)$. In particular, the G sum in V_{lr} has been truncated at $G = 12/b$ and a sufficient number of images in V_{sr} has been included, so that the overall error in the tabulation is less than $10^{-6} Ryd^*$.

III. WAVE FUNCTION

The wave function Ψ_T we used in our QMC simulations is of the Slater-Jastrow type:

$$\Psi_T = \exp\left(- \sum_{i<j} u(x_{ij})\right) D^\dagger D^\downarrow, \quad (10)$$

where D^σ is a determinant of N^σ plane waves with wave vectors occupied up to the Fermi momentum $k_F = \frac{\pi}{4r_s}$. The Jastrow factor contributes significantly to improve the quality of the variational state, since it correlates the particles and tunes the amplitude of Ψ_T . Here we use a two body Jastrow factor, which takes into account the electron-electron correlation, without spoiling the translational invariance of the system. A recent work³³ on the 1D $t - t'$ Hubbard model has shown that the long-range behavior of the two body Jastrow effectively accounts for the proper description of the metallic and insulating phases of that lattice model. Therefore a good functional form of $u(x)$ in Eq. 10 is crucial to obtain the correct physics for a strongly correlated 1D system.

In order to avoid spin contamination³⁴, the function $u(x)$ does not depend on the spin of the particles. In particular, we choose the RPA form of $u(x)$ as our first variational ansatz. Following Ref. 35, the Fourier components of u are:

$$2\rho u_{RPA}(k) = -S_0(k)^{-1} + \sqrt{S_0(k)^{-2} + 2\rho V_b(k)/k^2}, \quad (11)$$

with $S_0(k) = (k/2k_F)\theta(2k_F - k) + \theta(k - 2k_F)$ the structure factor of a non interacting one dimensional electron

gas (1DEG). The two body Jastrow is repulsive at the origin, to reduce the probability of two electrons to approach each other, and lower in this way the potential energy. Since the effective Coulomb coupling increases as the density decreases, the lower is the density, the higher is the Jastrow repulsion.

Rescaling u_{RPA} is the most straightforward improvement beyond the RPA ansatz. It improves the variational wave function by means of the simple parametrization

$$u(x) = \gamma u_{RPA}(x), \quad (12)$$

where γ is a linear parameter that we optimized using the variance minimization^{36,37}. The optimal values for γ are reported in Tab. I for different densities and for $N = 22$: the RPA seems good for the highest densities, where $\gamma \simeq 1$, but it becomes worse for lower densities, where the rescaling is effective. Indeed, whenever the correlation is stronger, u_{RPA} overestimates the interelectron repulsion. Moreover we have found that the optimal value of γ does not depend on the number of particles in the supercell, the function u_{RPA} having the proper dependence on N .

TABLE I: Scaling parameter γ of the u_{RPA} function optimized using the method of variance minimization for the 1DEG with $b = 0.1$ and $N = 22$

| | $r_s = 1$ | $r_s = 2$ | $r_s = 4$ | $r_s = 6$ | $r_s = 10$ |
|------------|-----------|-----------|-----------|-----------|------------|
| $ \gamma $ | 1.05 | 1.00 | 0.83 | 0.67 | 0.61 |

With the aim to check whether the scaled RPA is accurate enough to yield the correct Jastrow correlation for the lowest densities, when the effective coupling is higher, we take into account the most general expression for the two body Jastrow. We expand u in a linear sum of Chebyshev polynomials³⁸, which are a complete basis set in the orthogonality interval $(-1, 1)$:

$$u(x) = \sum_{m>0} \alpha_m T_{2m}\left(\frac{x - \frac{L}{2}}{\frac{L}{2}}\right), \quad (13)$$

where the range $(0, \frac{L}{2})$ is mapped into the interval $(-1, 0)$ and only the even polynomials are used. In this way the condition $u'(L/2) = 0$ is fulfilled, and ensures the continuity of the first derivative of u at the edge of the supercell. Moreover the sum in Eq. 13 starts from $m = 1$, since

T_0 is the identity and the wave function is determined apart from a constant. Using the variance minimization, we optimize the parameters α_m up to the convergence of the expansion in Eq. 13, which has been reached for $m = 10$. The variational energies relative to the various functional forms of u for $r_s = 10$ and $N = 22$ are summarized in Tab. II, whereas the functions are plotted in Fig. 1. The comparison shows that the scaled RPA Jastrow factor leads to a very good variational state, as its energy is very close to the exact GS value (more than 99.5% of correlation energy is recovered) and it is almost coincident to the most flexible variational form obtained with the mentioned Chebyshev expansion. The simple RPA form is a good approximation, since it provides a large fraction of the correlation energy (98.3%), but the rescaling of the RPA Jastrow yields a further substantial improvement. Thus it is clear that the most convenient parametrization of the Jastrow term is the scaled u_{RPA} , because one is able to reach an almost exact wave function already at the variational level, by optimizing just one variational parameter. For the above reason, in the forthcoming sections we will use the optimized and rescaled RPA Jastrow as trial wave function Ψ_T for all densities (r_s) and sizes (N) taken into account in this QMC study of the 1DEG.

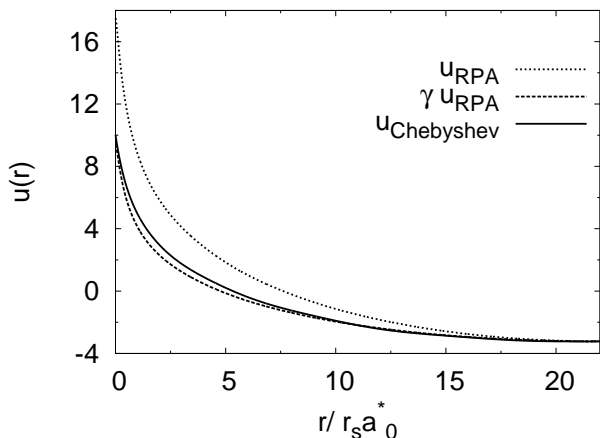


FIG. 1: Optimized u functions for $r_s = 10$ and $N = 22$: $u_{RPA}(x)$ (dotted line), $\gamma u_{RPA}(x)$ (dashed line), and the Chebyshev expansion for $u(x)$ (solid line). $r_s a_0^*$ is the unit length.

IV. LATTICE REGULARIZED DIFFUSION MONTE CARLO METHOD

The low dimensionality and the strong correlation among the electrons not only have dramatic consequences on the physical properties of the quantum wire, which will be studied in Secs. V and VI, but also affect the efficiency of the QMC simulations of the system. Indeed, as we have seen in the previous section, the effective

TABLE II: Total energy E_{tot} , correlation energy E_{corr} and percentage of correlation energy $\%E_{corr}$ for $b = 0.1$, $r_s = 10$, and $N = 22$. The fraction of the correlation energy recovered is computed from LRDMC calculations which provide the exact GS energy for a 1DEG (see Sec. IV).

| | E_{tot} | E_{corr} | $\%E_{corr}$ |
|------------|--------------|--------------|--------------|
| RPA | -0.47207(2) | -0.20519(56) | 0.9830(15) |
| Scaled RPA | -0.474825(9) | -0.20794(55) | 0.9962(15) |
| Chebyshev | -0.474900(9) | -0.20802(55) | 0.9965(15) |

Coulomb interaction leads to an optimal wave function with a strong repulsive Jastrow factor, which freezes the relative positions of the particles and enhances the $2k_F$ component of the charge-charge correlation, a signature that the system is close to the Wigner phase. The two body Jastrow, necessary to provide a good variational description of the system, introduces *pseudo nodes*, i.e. surfaces in the configuration space where the wave function almost vanishes, due to the exponential increase of $J(x)$, which acts like a Gutzwiller projector, by avoiding “double” occupancies on a given electronic position x . These *pseudo nodes* are similar to the usual nodes of the fermionic wave function, but if the latter arise from the antisymmetrization of the many body state, the former are a consequence of the strong repulsion, which prevents two electrons to come closer and eventually overlap. The effect of the *pseudo nodes* on the QMC simulation is harmful, since in the 1D case they can lead to a slow convergence of the Markov chain to the equilibrium distribution. In particular, it can be extremely difficult to connect two configurations with a spin exchange. However, the charge degrees of freedom are still well reproduced in spite of this lack of ergodicity, as one might infer that the pseudo nodal pockets are equivalent for the charge properties. Instead the expectation values of spin dependent operators are spoiled, if the Markov chain is not able to guarantee a sufficient number of spin exchanges during the simulation in a reasonable time.

The variational Monte Carlo (VMC) algorithm can easily overcome the problem, since the proposed move can be forced to flip the spin of an electronic configuration, either by explicitly introducing a spin exchange or by allowing the amplitude of the move to be greater than the mean interparticle distance. Instead in the diffusion Monte Carlo (DMC) approach, the random walk has to follow the diffusion process driven by the imaginary time dependent Schrödinger equation. If the importance sampling is introduced, the resulting Green function, approximated by means of the Trotter expansion up to the first order in the time step τ , includes the drift-diffusion dynamics:

$$\mathbf{R}' = \mathbf{R} + D\tau\nabla \ln |\Psi_T(\mathbf{R})|^2 + \chi\sqrt{2D\tau}, \quad (14)$$

where $\nabla \ln |\Psi_T(\mathbf{R})|^2$ is the quantum force, $D = 1$ is the diffusion coefficient, and χ is a Gaussian distributed random variable. The configurations generated step by step

are distributed accordingly to $|\Psi_T|^2$ at the beginning of the simulation, but after a transient they will reach the equilibrium and sample the mixed distribution $\Psi_{FN}\Psi_T$, where Ψ_{FN} is the lowest variational state with the same nodes as the trial wave function Ψ_T (this is the so called fixed node (FN) constraint). In order to get rid of the time step bias in the final result, one needs to extrapolate the FN energies obtained at different time steps for τ going to zero. For smaller τ , spin exchanges become rarer, because the mean square displacement vanishes linearly with τ (Eq. 14). To overcome the lack of spin exchanges in the DMC, we have applied a different projection QMC method, the lattice regularized Green function Monte Carlo (LRDMC), successfully introduced in Ref. 29 to cure the localization error in the presence of non local potentials. In this section we review the method and compare its efficiency of sampling spin flips with respect to the standard DMC framework.

The main idea behind the LRDMC method is to deal with a regularized Hamiltonian in such a way that the standard Green function Monte Carlo (GFMC) algorithm^{39,40,41} on a lattice can be applied also to continuous systems. The regularization of the Hamiltonian in Eq. 2 involves both the kinetic and the potential parts. The Laplacian is discretized by means of the finite differences

$$\Delta = \eta \left[p\Delta^a + (1-p)\Delta^{a'} \right] + O(a^2), \quad (15)$$

with Δ^a an Hermitian lattice operator given by

$$\Delta^a \Psi(x_i) = \frac{1}{a^2} (\Psi(x_i + a) + \Psi(x_i - a) - 2\Psi(x_i)), \quad (16)$$

where a is the mesh size, p and η are constants ($\eta = 1 + O(a^2)$), and x_i is the position of the i -th electron. Due to the homogeneity of the system, p is kept spatially independent, contrary to the general case²⁹ where the dependence of p on the electronic positions is exploited to improve the efficiency of the diffusion process. Here $p = 0.5$, and the contributions to the total Laplacian coming from Δ^a and $\Delta^{a'}$ are equally weighted. The two terms, with $a'/a = \sqrt{5}$, allow the diffusion to explore all the continuous space, since the two meshes are incommensurate; in this way the lattice space bias due to the discretization of the continuous kinetic operator is greatly reduced and one can work with a reasonably large value of a without a significant lattice step error.

Also the potential is regularized, so that our final Hamiltonian H^a fulfills the following three conditions: i) $H^a \rightarrow H$ for $a \rightarrow 0$; ii) for the chosen trial wave function Ψ_T , for any a and any configuration x , the local energy $e_L(\mathbf{R}, [\Psi_T]) = \frac{H\Psi_T(\mathbf{R})}{\Psi_T(\mathbf{R})}$ of the continuous Hamiltonian H is equal to the one $e_L^a(\mathbf{R}, [\Psi_T])$ corresponding to the Hamiltonian H^a ; iii) the discretized kinetic energy is equal to the continuous one calculated on the state Ψ_T . The condition (iii) determines the constant η , while the condition (ii) fixes the form of the regularized potential

V^a :

$$V^a(\mathbf{R}) = V(\mathbf{R}) + \frac{1}{2} \left[\frac{\sum_i (\Delta_i^a - \Delta_i) \Psi_T}{\Psi_T} \right] (\mathbf{R}). \quad (17)$$

Notice that the condition (ii) yields another important property for H^a : if Ψ_T is an eigenstate of H , it is also an eigenstate of H^a for any a . Thus, as the quality of Ψ_T increases, the dependence of the LRDMC energy on a decreases.

The lattice regularized Hamiltonian H^a reads:

$$H_{\mathbf{R}', \mathbf{R}}^a = \begin{cases} -\eta p/a^2 & \text{if } \mathbf{R}' = \mathbf{R} + \delta_a \\ -\eta (1-p)/a'^2 & \text{if } \mathbf{R}' = \mathbf{R} + \delta_{a'} \\ 2N\eta \left(\frac{p}{a^2} + \frac{1-p}{a'^2} \right) + V^a(\mathbf{R}) & \text{if } \mathbf{R}' = \mathbf{R}, \end{cases} \quad (18)$$

where δ_a ($\delta_{a'}$) is a N dimensional vector defined as the *one* particle displacement of length $\pm a$ ($\pm a'$). Thus there are $2N$ different δ_a ($\delta_{a'}$), and H^a in Eq. 18 contains $4N$ off diagonal elements, which come from the discretization of the Laplacian (Eq. 15). In particular, by defining the importance sampling Green function, $G_{\mathbf{R}', \mathbf{R}} = \Psi_T(\mathbf{R}')(\Lambda\delta_{\mathbf{R}', \mathbf{R}} - H_{\mathbf{R}', \mathbf{R}})/\Psi_T(\mathbf{R})$, the configuration \mathbf{R} is connected by $G_{\mathbf{R}', \mathbf{R}}$ to a *finite* number of configurations \mathbf{R}' , although \mathbf{R} and \mathbf{R}' live in a continuous space. Therefore the Green function $G_{\mathbf{R}', \mathbf{R}}$ is *discrete*, and can be sampled using a heat bath algorithm, like in the standard GFMC scheme on a lattice, although in this case \mathbf{R} and \mathbf{R}' are continuous variables. Another important difference with respect to the lattice case is the spectrum of H^a , which is unbounded from above; thus, in order to guarantee the positivity of the Green function, we need to perform the limit $\Lambda \rightarrow \infty$, which can be handled within the continuous time formulation, already introduced in Ref. 41 for the GFMC method.

Although in the continuous limit $a \rightarrow 0$ there is no sign problem because the sampling is restricted within a region -the nodal pocket- with definite sign, for non zero a the fermionic sign problem is still present and needs to be treated by means of an effective Hamiltonian³⁹, which approximates the regularized H^a (FN constraint). The regularized effective Hamiltonian H^{eff} included in the LRDMC algorithm is defined as follows:

$$H_{\mathbf{R}', \mathbf{R}}^{\text{eff}} = \begin{cases} H_{\mathbf{R}, \mathbf{R}'}^a & \text{if } \mathbf{R} \neq \mathbf{R}' \text{ and} \\ & \Psi_T(\mathbf{R}')H_{\mathbf{R}, \mathbf{R}'}^a/\Psi_T(\mathbf{R}) \leq 0 \\ 0 & \text{if } \mathbf{R} \neq \mathbf{R}' \text{ and} \\ & \Psi_T(\mathbf{R}')H_{\mathbf{R}, \mathbf{R}'}^a/\Psi_T(\mathbf{R}) > 0 \\ H_{\mathbf{R}, \mathbf{R}}^a + \mathcal{V}_{sf}(\mathbf{R}) & \text{if } \mathbf{R} = \mathbf{R}', \end{cases} \quad (19)$$

where $\mathcal{V}_{sf}(\mathbf{R}) = \sum_{\mathbf{R}' \neq \mathbf{R}} \Psi_T(\mathbf{R}')H_{\mathbf{R}', \mathbf{R}}^a/\Psi_T(\mathbf{R}) > 0$, the so called sign-flip term, is the sum over all the terms that cause a negative sign problem in the Monte Carlo sampling. For this reason these terms are traced in the diagonal part of the effective Hamiltonian, that therefore no longer contains off diagonal terms with the "wrong" sign. The ground state Ψ_{FN} of H^{eff} has the same signs as the trial wave function Ψ_T , and so the mixed distribution $\Psi_{FN}\Psi_T$ sampled during the LRDMC simulation

will be non negative. In general, in the limit $a \rightarrow 0$ the FN energy $E_{FN} = \langle \Psi_{FN} | H^{\text{eff}} | \Psi_T \rangle$ of the effective Hamiltonian H^{eff} is an upper bound of the GS energy E_0 of H . The FN approximation turns out to be exact only if the nodes of the trial wave function are the same as the GS nodes. However, the trial wave function Ψ_T in Eq. 10 has the exact GS nodes. Indeed in the 1D case the nodal structure of the GS is exactly defined by the coalescence planes $x_i = x_j$, where x_i and x_j are two electrons with the same spin, and the position of the planes are completely determined by the antisymmetry of the particles²⁶. Therefore both the LRDMC ($a \rightarrow 0$) and DMC ($\tau \rightarrow 0$) values for this 1D system are exact within their statistical precision.

We did an accurate comparison between the DMC and LRDMC approaches, by taking into account the efficiency of the energy estimate, the dependence on the time step and on the lattice space, and the spin flip frequency during the simulations, defined as the number of exchanges between two particles with opposite spin per unit time (imaginary projection time) per particle. The “standard” DMC algorithm, taken as the reference for our comparison, is described in Ref. 42. We applied the two QMC schemes to the quantum wire model with $N = 22$ and for r_s ranging from 1 to 10. For a fair comparison, we chose the DMC time step $\tau = a^2/2$, so that both algorithms provide the same amplitude for the diffusion move. The efficiency of the DMC energy estimate is double that of the LRDMC, since in the latter approach we need to compute in advance all the possible off diagonal moves, thus losing a fraction of the computing time. On the other hand, as reported in Table III, the spin exchange frequency is almost the same for the high density model, when the correlation is weak, but the LRDMC becomes more and more effective in sampling the spin flips when the density is lower and the correlation becomes stronger. In particular, for the lowest density ($r_s = 10$) the LRDMC algorithm yields an efficiency in the spin flip sampling which is two orders of magnitude higher than the DMC case.

Another appealing behavior of the LRDMC approach is the lattice space dependence of the fixed node energy. As one can see in Fig. 2, the LRDMC energies have a quadratic dependence on a with a prefactor much smaller than the slope of the linear fit for the corresponding DMC energies. This means that in order to obtain an almost converged LRDMC result one does not need to go to small lattice spaces, with a gain both from the computational point of view and from the efficiency in the spin flip sampling, which of course is reduced as the diffusion move goes to zero.

To summarize, it is apparent that both the lattice step bias and the lack of ergodicity are greatly reduced by using the LRDMC algorithm in the place of the standard DMC. Therefore, given the amplitude of the QMC move, the LRDMC is more effective than the DMC scheme. We believe that the reason is related to the Trotter approximation behind the DMC propagator, which spoils the

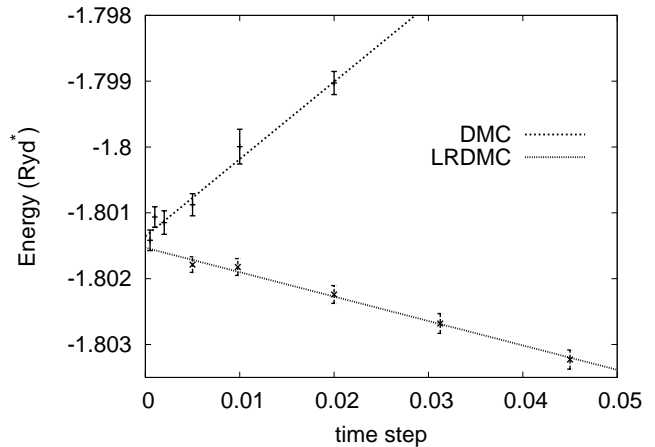


FIG. 2: DMC and LRDMC energies dependence on the time step ($b = 0.1, r_s = 1, N = 22$). The lattice space a has been mapped into the time step, by means of the relation $a = \sqrt{2\tau}$. For both the two cases, the dependence appears to be linear, with a slope of 0.117(8) for the DMC algorithm and -0.018(2) for the LRDMC approach.

exact dynamics of the diffusion process and apparently affects the ergodicity of the random walk. On the other hand, even within a finite lattice space, the LRDMC algorithm converges to the exact GS of the effective Hamiltonian H^{eff} in Eq. 19, implying that simulations are always physically meaningful even for $a > 0$. This should allow in general a more controlled and smooth extrapolation to the continuous $a \rightarrow 0$ limit.

In the next section, we will analyze both the VMC and the LRDMC results for the quantum wire model. For every density and width, we have performed a lattice space extrapolation ($a \rightarrow 0$) and a finite size extrapolation to the thermodynamic limit ($N \rightarrow \infty$). To extrapolate the energies to the continuous limit, we have fitted points computed in the range $0.05 \leq a \leq 1.2$ with a quadratic function in a , as reported in Fig. 2, while for the extrapolation to the thermodynamic limit we used the function $E_\infty + c_1/N + c_2/N^2$ in our fits. We evaluated the LRDMC energies for $N = 10, 22, 42, 62, 82$, but in some cases, for low r_s , we carried out LRDMC simulations with as many as 242 particles, in order to have always a reliable estimate of the finite size errors.

V. CORRELATION ENERGY

The correlation energy per particle $E_{\text{corr}} = E_0 - E_{\text{HF}}$ is computed for various values of the width parameter b and densities r_s , and parametrized as a function of r_s for each b . The unpolarized HF energy of this quantum wire model is

$$E_{\text{HF}}(r_s, b) = \frac{\pi}{48r_s^2} + F\left(\frac{\alpha r_s}{2b}\right)/b, \quad (20)$$

TABLE III: Spin exchange frequency (Ryd^*) for the LRDMC and DMC algorithm at different densities for the quantum wire model with $N = 22$ and $b = 0.1$. Notice that the frequency is reduced when the density decreases, while the efficiency of the LRDMC increases with respect to the DMC. All the simulations have been performed with $a = 0.2r_s$ and $\tau = a^2/2$.

| | $r_s = 1$ | $r_s = 2$ | $r_s = 4$ | $r_s = 6$ | $r_s = 10$ |
|---------|-----------|----------------------|----------------------|----------------------|----------------------|
| LRDMC | 1.18 | $5.72 \cdot 10^{-2}$ | $1.96 \cdot 10^{-2}$ | $3.19 \cdot 10^{-4}$ | $8.86 \cdot 10^{-6}$ |
| DMC | 1.14 | $3.81 \cdot 10^{-2}$ | $4.24 \cdot 10^{-3}$ | $3.21 \cdot 10^{-5}$ | $9.09 \cdot 10^{-8}$ |
| rel eff | 1.03 | 1.50 | 4.62 | 9.94 | 97.47 |

where the first term is the kinetic energy, and the second contribution is the exchange energy (E_{ex}) term with $\alpha = 4/\pi$ and the function F defined by

$$F(R) = -\frac{1}{2\pi} \int_0^{1/R} dx f(x) [1 - Rx]. \quad (21)$$

The Hartree term vanishes since the system is neutral and homogeneous.

We evaluated the GS energy E_0 using the LRDMC method with the FN approximation, which projects the initial Ψ_T to the lowest energy state of the system with the same nodes of Ψ_T . However, since the trial wave function in Eq. 10 has the exact GS nodes, our LRDMC energies are exact within their statistical precision in the limit $a \rightarrow 0$, as already pointed out in Sec. IV. The correlation energy is then obtained by subtracting the HF energy of Eq. 20 from the GS energy. Thus, the correlation energy is computed exactly for a given value of r_s and b .

It is useful to study the correlation energy in the high and low density limits, in order to find a good parametrization which includes the correct asymptotic behavior. In the high density limit, i.e. $r_s \rightarrow 0$, the correlation energy can be computed via a perturbative expansion of the interaction, using the RPA technique to find the coefficient of the lowest order term in r_s (see Appendix A). It turns out that the correlation energy is quadratically vanishing, as r_s goes to zero

$$E_{corr}(r_s \rightarrow 0) = -\frac{A_{corr}}{\pi^4 b^2} r_s^2, \quad (22)$$

where $A_{corr} = \int_0^\infty dx x f(x)^2 = 4.9348$. This result was obtained by Calmels and Gold, using the mean spherical approximation (MSA)^{22,23}, which is consistent with the RPA finding. On the other hand, in the low density regime ($r_s \rightarrow \infty$) the exact behavior of E_{corr} can be guessed by studying the ratio E_{corr}/E_{ex} . For instance, in Ref. 22 the correlation was computed using a three-sum-rule approach (3SRA) of the STLS theory for the same model, and this ratio turned out to be

$$\frac{E_{corr}(r_s \rightarrow \infty)}{E_{ex}(r_s \rightarrow \infty)} = 0.84. \quad (23)$$

Since the asymptotic expansion of $E_{ex}(r_s)$ in the limit of $r_s \rightarrow \infty$ is²²

$$E_{ex}(r_s) \simeq -\frac{\ln(r_s)}{r_s} \left(\frac{1}{2} + O\left(\frac{1}{\ln(r_s)}\right) \right), \quad (24)$$

it is possible to obtain an asymptotic estimate also for $E_{corr}(r_s \rightarrow \infty)$. One can perform the same comparison using the LRDMC data. In Fig.3 the value of E_{corr}/E_{ex} is reported as function of r_s for all b studied ($b = 0.1, 0.3, 0.5, 0.75, 1, 2, 4$). The points have been fitted using the following function:

$$\frac{E_{corr}(r_s)}{E_{ex}(r_s)} = \tilde{a} + \frac{\tilde{b}}{\ln(r_s)} + \frac{\tilde{c}}{r_s}, \quad (25)$$

where \tilde{a} , \tilde{b} , and \tilde{c} are fitting parameters. According to Eq. 24, the slowest decaying contribution to E_{corr}/E_{ex} should be $\propto 1/\ln(r_s)$, which has been included in the fit. Therefore an accurate extrapolation to $r_s \rightarrow \infty$ is very difficult, since the logarithmic correction in the low density regime is extremely slow, and in order to have a reliable estimate of \tilde{a} , one should compute the correlation energy at much higher values of r_s . For instance, in the 3SRA-STLS theory²², the ratio E_{corr}/E_{ex} converges to the value in Eq. 23 for $r_s > 1000$, which is of course a regime where the QMC framework is not ergodic. In any case, in the range of densities from $r_s = 15$ to $r_s = 50$ (the lowest density taken into account) the function in Eq. 25 fits well our data points, apart from the case with $b = 4$, which requires even lower densities to enter into its asymptotic regime. In our fits, \tilde{a} assumes values ranging from 1.0 to 1.1, which are slightly larger than those yielded by the STLS theory. Thus also our data seem to support the idea that the correlation energy in quasi-one dimensional systems behaves as

$$E_{corr}(r_s \rightarrow \infty) \propto -\frac{\ln(r_s)}{r_s}, \quad (26)$$

or at least this behavior is compatible with our data until $r_s = 50$.

A good parametric representation of the correlation energy has to satisfy the asymptotic behavior both at $r_s = 0$ and $r_s = \infty$. Agosti *et al.*⁴³ used the interpolation formula

$$\epsilon(r_s) = \frac{r_s^p}{C + Dr_s^q}, \quad (27)$$

with p , q , C , and D variational parameters, in order to fit their STLS data for a similar 1DEG model system (with hard confinement of a 2DEG in one direction). They found the above function fits correlation energies very well in the intermediate range of densities, but it is apparent that their expression does not yield the ‘‘exact’’

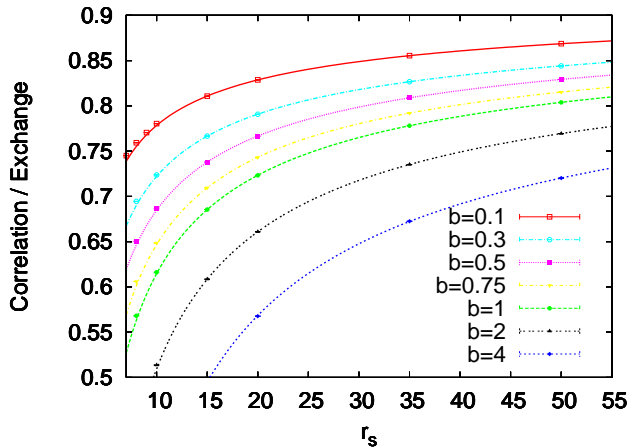


FIG. 3: (Color online) Values of E_{corr}/E_{ex} plotted versus r_s in the low density regime for various thickness b . The curves are obtained from a fit of the LRDMC points using the function in Eq. 25 in the range $15 \leq r_s \leq 50$.

asymptotic behavior at high and low densities. Here we give a simple analytic representation of the correlation energy which fits our simulation data over a wide range of densities (from $r_s = 0.05$ to $r_s = 50$) and for different values of lateral confinement. Moreover it includes the correct low and high density limits. Following the same lines as Perdew-Wang⁴⁴ and Attaccalite *et al.*⁴⁵, we use a parametric function which reads

$$\epsilon(r_s) = -\frac{r_s}{A + Br_s^n + Cr_s^2} \ln(1 + \alpha r_s + \beta r_s^m). \quad (28)$$

The total number of parameters is 7: 3 linear coefficients (A , B , and C) and one exponent ($0 < n < 2$) for the polynomial part, 2 linear coefficients (α , and β) and one exponent ($m > 1$) in the argument of the logarithm. The high density limit of the parametrization is

$$\epsilon(r_s \rightarrow 0) = -\frac{\alpha}{A} r_s^2, \quad (29)$$

and its low density limit is

$$\epsilon(r_s \rightarrow \infty) = -\frac{m}{C} \frac{\ln(r_s)}{r_s}. \quad (30)$$

Thus the expected behavior of the correlation energy is correctly reproduced by our parametric form (Eq. 28) for both the high and low density limits. In order to obtain a priori the exact high density result (Eq. 22) known from the RPA theory (see Appendix A), we fix the ratio α/A to be equal to $A_{corr}/(\pi^4 b^2)$. Therefore the number of independent parameters in the function (28) is reduced to 6. In particular, we determine A from the high density limit, while the other parameters are free to minimize the χ^2 . Their optimal values are listed in Tab. IV.

We define the accuracy η of the parametrization by

$$\eta = \frac{1}{M} \sum_{i=1}^M |E_{corr}(i) - \epsilon(i)|, \quad (31)$$

where M is the total number of r_s points computed for a given b . In practice, η is the average of the residuals and measures the discrepancy between the computed value E_{corr} and its parametric value ϵ . The order of magnitude of the accuracy η is between $10^{-4} Ryd^*$ and $10^{-5} Ryd^*$, depending on the thickness of the wire. It means that the parametrization is very accurate in the range of density with $0 < r_s < 50$ and for values $0.1 \leq b \leq 4$ of the width parameter. In Fig. 4 we plot the points and the parametrization curves for the correlation energy in the range of density and width taken into account. Notice that the thinner is the wire, the more correlated is its ground state.

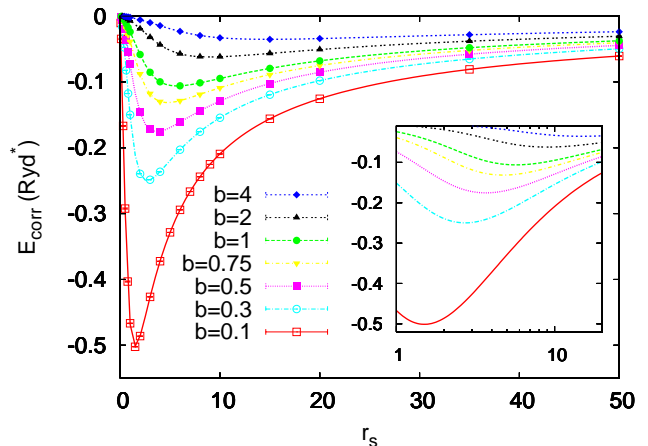


FIG. 4: (Color online) Correlation energy versus the density parameter r_s . The points are the LRDMC data used in the fit. Their dimension is much bigger than the error bars. We computed the LRDMC correlation energy at $r_s = 0.1, 0.2, 0.3, 0.4, 0.6, 0.8, 1, 2, 3, 4, 6, 8, 10, 15, 20, 35, 50$. The curves are the parametrization of the correlation energy for various values of the width parameter b . In the inset, the semi-log plot magnifies the region around the minimum of the energy correlation functional.

To conclude this section, in Fig. 5 we compare our LRDMC results with those obtained by Calmels and Gold using the 3SRA approach²². The relative difference between the two methods is about 20% around the minimum, where the absolute value of the correlation energy is larger. The STLS method with the 3SRA sum rule is able to yield a large fraction (80% or more) of the correlation energy. However our results, which are formally exact, represent a further improvement with respect to the previous estimate of the correlation energy for this model quantum wire.

VI. PAIR CORRELATIONS

In this section we study the density-density and spin-spin correlation functions, which are useful quantities for assessing the nature of the ground state of the system. We first analyze the charge $g_{\rho\rho}(r)$ and spin $g_{\sigma\sigma}(r)$ pair

TABLE IV: Optimal fit parameters for the correlation energy, as parametrized in Eq. 28. Different values of b are taken into account, for each of them we give its parametrization. In the last rows, we report the reduced χ^2 and the overall numerical accuracy η in Ryd^* , defined in Eq. 31. A has been determined from the high density limit 22, which is therefore exactly fulfilled by our fit. The error of the parameters in the last digits is reported in parenthesis.

| | $b = 0.1$ | $b = 0.3$ | $b = 0.5$ | $b = 0.75$ | $b = 1.0$ | $b = 2.0$ | $b = 4.0$ |
|----------|---------------------|---------------------|---------------------|---------------------|---------------------|---------------------|---------------------|
| A | 4.66(5) | 9.50(9) | 16.40(11) | 22.53(24) | 32.1(1.3) | 110.5(2.8) | 413.0(5.9) |
| B | 2.092(24) | 1.85(17) | 2.90(13) | 2.09(12) | 3.77(23) | 7.90(49) | 10.8(7) |
| C | 3.735(34) | 5.64(8) | 6.235(46) | 7.363(44) | 7.576(36) | 8.37(6) | 7.99(20) |
| n | 1.379(10) | 0.882(13) | 0.908(7) | 0.906(8) | 0.941(49) | 1.287(26) | 1.549(35) |
| α | 23.63(26) | 5.346(53) | 3.323(22) | 2.029(22) | 1.63(7) | 1.399(35) | 1.308(19) |
| β | 109.9(5.5) | 6.69(43) | 2.23(7) | 0.394(12) | 0.198(8) | 0.0481(19) | 0.0120(9) |
| m | 1.837(18) | 3.110(42) | 3.368(23) | 4.070(30) | 4.086(21) | 4.260(25) | 4.165(40) |
| χ^2 | 4.4 | 9.4 | 15.7 | 8.9 | 5.7 | 6.0 | 15.7 |
| η | $5.0 \cdot 10^{-4}$ | $5.4 \cdot 10^{-4}$ | $3.4 \cdot 10^{-4}$ | $1.1 \cdot 10^{-4}$ | $5.7 \cdot 10^{-5}$ | $5.4 \cdot 10^{-5}$ | $4.4 \cdot 10^{-5}$ |

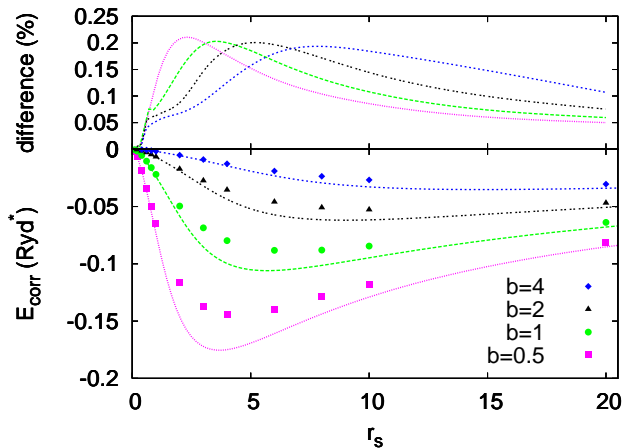


FIG. 5: (Color online) In the lower panel, we plot the correlation energy obtained by Calmels and Gold²² (points) and the parametrization of our LRDMC data (curves) for various values of the width parameter b . In the upper panel, we compute the relative difference $|\epsilon - E_{Calmels}|/\epsilon$ interpolated all over the density range taken into account.

correlations, defined as

$$g_{\rho\rho}(r) = 1/2 (g_{\uparrow\uparrow}(r) + g_{\downarrow\downarrow}(r)), \quad (32)$$

$$g_{\sigma\sigma}(r) = 1/2 (g_{\uparrow\uparrow}(r) - g_{\downarrow\downarrow}(r)),$$

where we used the spin resolved pair distribution function

$$g_{\alpha\beta}(r) = \frac{1}{L\rho_{\alpha\rho\beta}} \sum_{i \neq j} \langle \delta(r_i^\alpha - r_j^\beta - r) \rangle, \quad (33)$$

with $\alpha, \beta = \uparrow, \downarrow$, and $\rho_\uparrow = \rho_\downarrow = \rho/2$ is the density of the two spin components in the unpolarized system. We computed $g_{\rho\rho}(r)$ and $g_{\sigma\sigma}(r)$ of the wires with thickness $b = 0.1$ and densities $r_s = 1, 2, 4$, by means of the LRDMC algorithm and the forward walking technique⁴⁰, which yields unbiased expectation values on the ground state of the system also for operators which do not commute with the Hamiltonian. The correlation functions are drawn in Figs. 6 and 7.

The charge-charge correlation functions in Fig. 6 reveal the strong effect of the electronic correlation in the

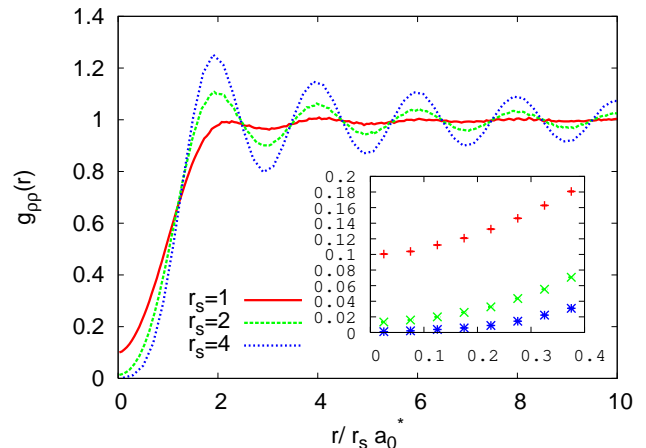


FIG. 6: (Color online) Charge-charge pair correlation function $g_{\rho\rho}(r)$ computed from LRDMC simulations with $b = 0.1$ and $N = 82$ at different densities. In the inset, the short-range part of $g_{\rho\rho}(r)$ is magnified.

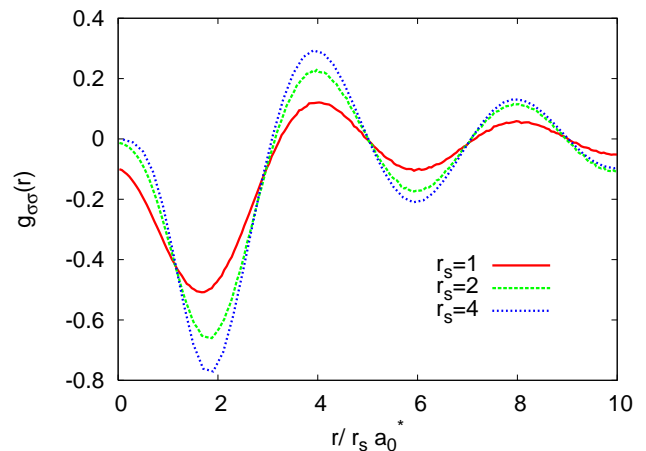


FIG. 7: (Color online) Spin-spin pair correlation function $g_{\sigma\sigma}(r)$ computed from LRDMC simulations with $b = 0.1$ and $N = 82$.

low density regime. As the density is decreased, the particles repel each other with an effective interaction which

is stronger. Consequently $g_{\rho\rho}(0)$ is smaller, as one can see in the inset of the Fig. 6. At the same time the fluctuations in the $g_{\rho\rho}(r)$ are larger, with periodicity $2r_s a_0^*$, and a slow decay. We will see however that this decay is not slow enough to give rise to a true long range order (Wigner crystal), since the quantum fluctuations will prevent the freezing of the charge in 1D. On the other hand, the short-range behavior of the spin-spin correlation functions in Fig. 7 shows the antiferromagnetic character of the coupling among electrons, and the underlying periodicity in the spin sector is $4r_s a_0^*$, i.e. twice the mean interparticle distance.

The analytical behavior of charge and spin correlations for the quasi 1D DEG with long range interaction has been obtained by Schulz¹⁶ using bosonization techniques applied to an effective one dimensional Hamiltonian with linearized kinetic energy. For that model Hamiltonian, it turns out that the charge correlation function exhibits a slow decay of its $4k_F$ component

$$\langle \rho(x)\rho(0) \rangle \simeq A \cos(4k_F x) \exp(-4c\sqrt{\ln(x)}), \quad (34)$$

with c an interaction dependent parameter. Its behavior has been related to a quasi order of the electrons, since in one dimension there is no true long-range order. Their fluctuations are almost frozen to maximize the interparticle distance along the wire, and their relative positions are pinned around lattice sites with periodicity $2r_s a_0^*$, exactly as we have seen in the $g_{\sigma\sigma}(r)$ for our model. The formation of this quasi Wigner crystal comes from the $1/r$ tail of the potential, since in the case of short-range interactions the $4k_F$ component of the charge correlation function decays much faster. On the other hand the spin correlation function has no singularity at $4k_F$ and exhibits the slowest decay for the $2k_F$ component. Indeed, according to the bosonization technique¹⁶, the large distance spin correlations are given by:

$$\langle \sigma(x)\sigma(0) \rangle \simeq B \cos(2k_F x) \exp(-c\sqrt{\ln(x)})/x, \quad (35)$$

where c is the same as in Eq. 34.

In order to check whether the Eqs. 34 and 35 are valid for our quantum wire model with long-range interactions and quadratic dispersion, we have also studied the charge $S_{\rho\rho}(k)$ and spin $S_{\sigma\sigma}(k)$ structure factors, defined as

$$\begin{aligned} S_{\rho\rho}(k) &= \langle \rho(k)\rho(-k) \rangle / N \\ S_{\sigma\sigma}(k) &= \langle \sigma(k)\sigma(-k) \rangle / N, \end{aligned} \quad (36)$$

where $\rho(k)$ ($\sigma(k)$) is the Fourier component of the local charge (spin) density. We have computed the structure factors at several k values for $b = 0.1$, $r_s = 1, 2, 4$, using $N = 10, 22, 42, 62, 82$ in the LRDMC calculations and $N = 10, 22, 42, 82, 162$ in the less expensive VMC calculations. In Figs. 8 and 9 we plot $S_{\rho\rho}(k)$ and $S_{\sigma\sigma}(k)$ for the LRDMC simulations with the largest number of particles ($N = 82$). While the spin-spin correlations show a peak at $k = 2k_F$, for the charge degrees of freedom the highest peak arises at $k = 4k_F$, which corresponds to the periodicity of the quasi Wigner crystal.

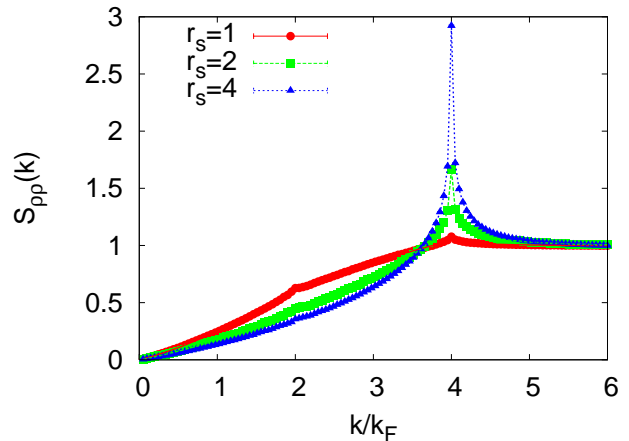


FIG. 8: (Color online) Charge structure factor $S_{\rho\rho}(k)$ computed from LRDMC simulations with $b = 0.1$ and $N = 82$.

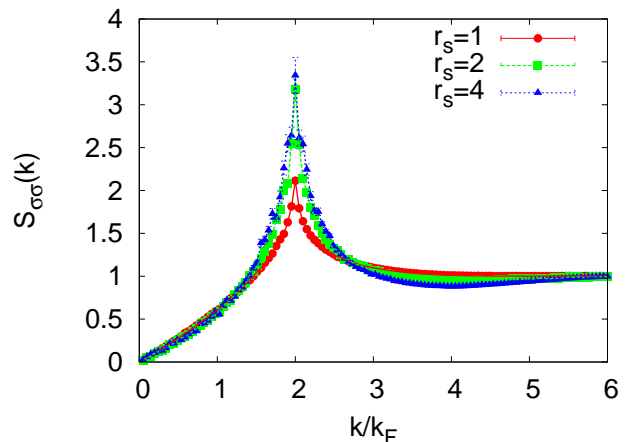


FIG. 9: (Color online) Spin structure factor $S_{\sigma\sigma}(k)$ computed from LRDMC simulations with $b = 0.1$ and $N = 82$.

In particular, we have studied the dependence of the peak heights $S_{\rho\rho}(4k_F, N)$ and $S_{\sigma\sigma}(2k_F, N)$ on the number of particles N , and compared it with the behavior predicted by the bosonization. From Eqs. 34 and 35, one can easily obtain⁴⁶:

$$\begin{aligned} S_{\rho\rho}(4k_F, N) &= a_1 L \exp(-4c\sqrt{\log L}) + a_2, \\ S_{\sigma\sigma}(2k_F, N) &= a_3(\sqrt{\log L}/c + 1/c^2) \exp(-c\sqrt{\log L}) \\ &\quad + a_4, \end{aligned} \quad (37)$$

with $L = 2r_s N$, a_1, a_2, a_3, a_4 model and density dependent parameters, and c the same as in the bosonization results. We have then used Eqs. 38 and 37 to fit our results, obtaining first a_1, a_2, c from the fit of $S_{\rho\rho}(4k_F, N)$ and then a_3, a_4 from $S_{\sigma\sigma}(2k_F, N)$, with c fixed by $S_{\rho\rho}(4k_F, N)$. In Figs. 10 and 11 we plot the curves which best interpolate the VMC and LRDMC values for $S_{\rho\rho}(4k_F, N)$ and $S_{\sigma\sigma}(2k_F, N)$.

Our VMC and LRDMC results seem consistent with the predictions of the bosonization, at least in the range

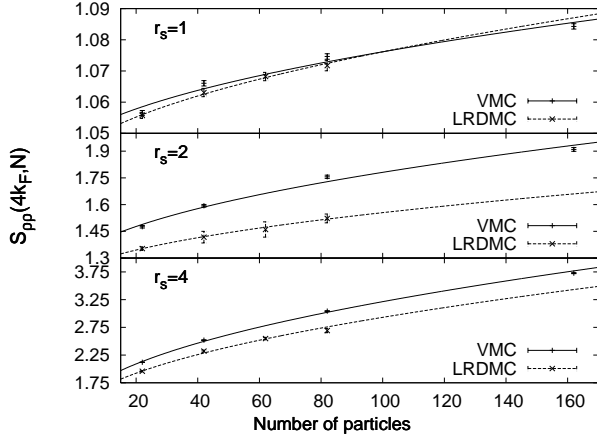


FIG. 10: Peak of the charge structure factor at $4k_F$ versus the system size for $r_s = 1, 2, 4$, $b = 0.1$, obtained from VMC and LRDMC calculations. The curves fit the points with function in Eq. 37.

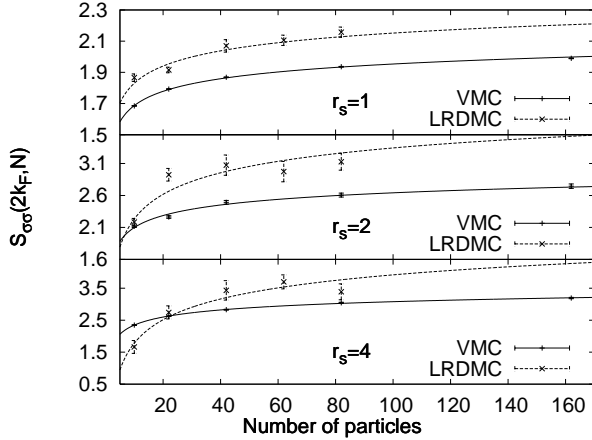


FIG. 11: Peak of the spin structure factor at $2k_F$ versus the system size for $r_s = 1, 2, 4$, $b = 0.1$, obtained from VMC and LRDMC calculations. The curves fit the points with function in Eq. 38.

of system sizes taken into account. As it is apparent from Figs. 10 and 11, the points are well fitted by Eqs. 37 and 38 respectively, the distance from the interpolating curves being usually less than 2 standard deviations. As already reported in Ref. 47, VMC results are in qualitative agreement with the bosonization findings, and the variational ansatz in Eq. 10 is good enough to capture the correct ground state properties. Indeed the LRDMC projection changes only quantitatively the VMC points, by reducing the charge structure factor, and by enhancing the spin structure factor, which however remains finite in the thermodynamic limit in accordance with Eq. 38. We emphasize once again that for this one dimensional system the LRDMC results are “exact” within their statistical accuracy, since the LRDMC yields the exact ground state energy *and* the points in Fig 10 and 11 are obtained

using the forward walking technique⁴⁰, which provides an unbiased expectation value for each correlation function.

The behavior of the spin and charge structure factor at small momenta reveals important features of the ground state, which are related to the low energy modes of the system. According to the bosonization results¹⁷, $S_{\rho\rho}(k)$ should behave as $\propto |k|/\sqrt{|\ln(k)|}$, while $S_{\sigma\sigma}(k)$ should go linearly with $|k|$. Our results are plotted in Figs. 12 and 13. In particular, in Fig. 12 we draw the renormalized

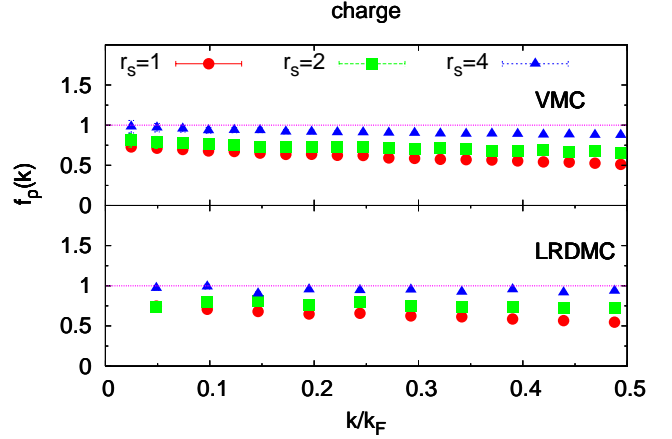


FIG. 12: (Color online) Plot of $f_\rho(k) = \frac{2}{\sqrt{r_s}} \frac{\sqrt{|\ln(k)|}}{k} S_{\rho\rho}(k)$ versus k/k_F for $r_s = 1, 2, 4$, $b = 0.1$, obtained from VMC ($N = 162$) and DMC ($N = 82$) calculations. The horizontal line is drawn as an eye guide.

charge structure factor $f_\rho(k) = \frac{2}{\sqrt{r_s}} \frac{\sqrt{|\ln(k)|}}{k} S_{\rho\rho}(k)$. Both the VMC and LRDMC data are in agreement with the small k limit of $S_{\rho\rho}(k)$:

$$\lim_{k \rightarrow 0} S_{\rho\rho}(k) = \alpha_g \frac{\sqrt{r_s}}{2} \frac{|k|}{\sqrt{|\ln(k)|}}, \quad (39)$$

where α_g is a factor which seems close to 1 and only slightly dependent on r_s , although the logarithmic behavior of $f_\rho(k)$ would require much smaller k in Fig. 12 in order to have an accurate extrapolation for α_g . Anyway, our result agrees at least qualitatively with the bosonization findings. Moreover, it is possible to derive analytically the behavior in Eq. 39 directly from our variational wave function Ψ_T , using the expression obtained by Reatto and Chester⁴⁸, that relates the small momenta behavior of $S_{\rho\rho}(k)$ with the 2-body Jastrow factor included in Ψ_T :

$$S_{\rho\rho}(k) \simeq \frac{S_0(k)}{1 + 2\rho u(k)S_0(k)}, \quad (40)$$

where $u(k)$ is the Fourier transform of the Jastrow function. The above relation is approximate for finite k , but it becomes exact to the leading order in k , for $k \rightarrow 0$, for the variational structure factor, i.e., for the one evaluated from the Slater-Jastrow trial function. After plugging the

definition of $u(k)$ (Eqs. 11 and 12) into the above equation, in the limit $k \rightarrow 0$ we have

$$S_{\rho\rho}(k) = \frac{1}{\gamma} \frac{\sqrt{r_s}}{2} \frac{|k|}{\sqrt{|\ln(k)|}}, \quad (41)$$

where γ is the parameter of the optimized RPA Jastrow factor. It is therefore clear that our choice of $u(k)$ satisfies the correct behavior of the charge structure factor already at the variational level, and the LRDMC simulations do not change this behavior (see Fig. 12). Moreover, from the knowledge of $S_{\rho\rho}(k)$ we can infer the behavior of the low energy charge excitations (plasmons) $\omega_\rho(k)$. Indeed, a variational estimate of $\omega_\rho(k)$ is given by (see Appendix B)

$$\omega_\rho(k) = \frac{k^2}{S_{\rho\rho}(k)}, \quad (42)$$

and in the limit $k \rightarrow 0$ it turns out that

$$\omega_\rho(k) = \frac{2}{\alpha_g \sqrt{r_s}} |k| \sqrt{|\ln k|}. \quad (43)$$

This expression should be compared with the low energy spectrum provided by bosonization studies^{16,49,50} of the Coulomb Luttinger liquid, which reads

$$\begin{aligned} \omega_\rho(k) &= v_\rho(k) |k|, \\ v_\rho(k) &= v_F \sqrt{(1+g_1)(1-g_1+2V(k)/\pi v_F)}, \end{aligned} \quad (44)$$

where v_ρ is the charge velocity, and g_1 is the amplitude of the backward scattering process. For small k excitations, we have

$$\lim_{k \rightarrow 0} \omega_\rho(k) = \sqrt{1+g_1} \frac{2}{\sqrt{r_s}} |k| \sqrt{|\ln k|}, \quad (45)$$

which corresponds to our findings in Eq. 43. Since in one dimension the long-wavelength spin and charge modes are independent, they have different velocities. This difference, due to the so-called spin-charge separation, has been seen in a remarkable experiment by Auslaender *et al.*⁴, and predicted by the Luttinger liquid theory. Indeed, according to this theory the spin excitations are

$$\omega_\sigma(k) = v_F \sqrt{1-g_1^2} |k|. \quad (46)$$

The spin dispersion is linear, since it is not affected by the long-range tail of the Coulomb interaction, in contrast to the charge velocity v_ρ , which is renormalized by the Fourier transform of the potential at small k . The linear behavior of the spin branch is reflected by the linear decay of $S_{\sigma\sigma}(k)$ as k goes to 0. In Fig. 13 we plot the renormalized spin structure factor $f_\sigma(k) = \frac{v_F}{k} S_{\sigma\sigma}(k)$ computed by carrying out both VMC and LRDMC simulations for $r_s = 1, 2, 4$. Since the value of $f_\sigma(k)$ is 1 in the limit of small k , it turns out that

$$S_{\sigma\sigma}(k) = \frac{k}{v_F}, \quad (47)$$

and it is the same behavior as the spin structure factor of a non-interacting gas. Therefore, the interaction leaves unchanged the $S_{\sigma\sigma}(k)$ tail at small k , which is another striking feature of the spin-charge separation. Notice that if we use $S_{\sigma\sigma}(k)$ to estimate the low lying spin-wave excitations (see Appendix B), we will obtain a spin velocity equal to v_F , and independent of r_s . This is of course a variational estimate, since the true spin velocity strongly depends on the density and is significantly reduced by the effective interaction²⁸, being equal to v_F only in the high density weak interaction regime.

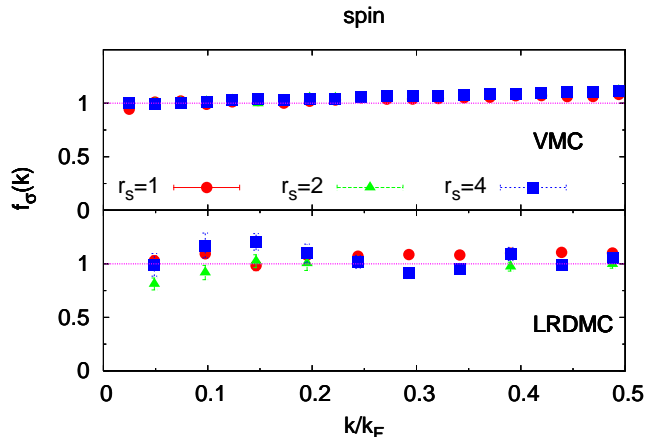


FIG. 13: (Color online) Plot of $f_\sigma(k) = \frac{v_F}{k} S_{\sigma\sigma}(k)$ versus k/k_F for $r_s = 1, 2, 4$, $b = 0.1$, obtained from VMC ($N = 162$) and DMC ($N = 82$) calculations. The horizontal line is drawn as an eye guide.

VII. CONCLUSIONS

In this paper we have carried out extensive Monte Carlo simulations to compute the ground state properties of the quantum wire model with unscreened long range interactions. We have used the novel LRDMC framework, which is shown to be more efficient than the standard DMC algorithm in the strong coupling regime, i.e. at low densities, when the exchange is extremely small and the features of a quasi-Wigner crystal are manifest. We computed the exact correlation energy, and found a simple and accurate parametrization, which fits the correlation energy over a wide range of electron densities and lateral confinements. This parametrization includes the correct behavior at high densities ($\epsilon(r_s \rightarrow 0) \propto r_s^2$), given by the RPA approximation. On the other hand, we guessed the asymptotic behavior at low densities from our data, and we found that $\epsilon(r_s \rightarrow \infty) \propto -\ln(r_s)/r_s$ fits well the LRDMC correlation energies in the strong coupling regime. We believe that our parametrization provides an extremely reliable functional for further DFT computations of quasi one dimensional systems. Last but not least, we showed that the pair correlations of

our model, exactly computed by means of LRDMC simulations and forward walking techniques, reproduce all features of the so-called Coulomb Luttinger liquid, i.e. a Luttinger liquid with linear dispersion and long-range Coulomb interaction. In particular, our results are compatible with the slow decay ($\propto \exp(-4c\sqrt{\ln(x)})$) of the spin structure factor at $4k_F$, which is the signature of a quasi order of the charge degrees of freedom. Moreover, the small k behavior of the static structure factor is in agreement with the bosonization findings, both for the charge and spin modes.

We plan to extend this study also to the spin polarized case, and to provide a spin resolved energy functional to be used as input of one dimensional DFT calculations with local spin density approximation.

Acknowledgments

We thank M. Fabrizio, C. J. Umrigar, D. M. Ceperley, S. Moroni and M. R. Geller for useful discussions. This work was partially supported by COFIN 2005, and CNR. One of us (M.C.) acknowledges support in the form of the NSF grant DMR-0404853.

APPENDIX A: RPA CALCULATION OF THE CORRELATION ENERGY

In this appendix, we compute the correlation energy in the high density limit using the random phase approximation (RPA). The RPA correlation energy reads⁵¹

$$\begin{aligned} E_{corr}^{RPA} &= \frac{L}{2\pi} \int_{-\infty}^{+\infty} dk E(k), \\ E(k) &= \frac{1}{4\pi} \frac{|k|}{N} \int_{-\infty}^{+\infty} d\lambda \ln(1 - v(kb)\chi^0(k, ik\lambda)) \\ &\quad + v(kb)\chi^0(k, ik\lambda), \end{aligned} \quad (A1)$$

where $v(kb)$ is the Fourier transform of the potential,

$$\chi^0(k, \omega) = \frac{1}{2\pi k} \ln \left(\frac{\omega^2 - (k^2 - v_F k)^2}{\omega^2 - (k^2 + v_F k)^2} \right), \quad (A2)$$

and the physical density-density response function of the free 1D electron gas is

$$\lim_{\eta \rightarrow 0^+} \chi^0(k, \omega + i\eta). \quad (A3)$$

Following the seminal work of Gell-Mann and Brueckner⁵², whose approach has also been used by Rajagopal and Kimball⁵³ for the 2D case, we define the so called electron-hole propagator

$$\begin{aligned} Q_q(u) &= \int_{-\infty}^{+\infty} dk \int_{-\infty}^{+\infty} dt f(k)(1 - f(k+q)) \\ &\quad e^{-it u q} \exp(-|t|(\frac{1}{2}q^2 + kq)), \end{aligned} \quad (A4)$$

where $f(x) = \theta(|x| - 1)$ is the zero temperature Fermi distribution, with θ the step function:

$$\theta(x) = \begin{cases} 1 & \text{if } x < 0 \\ 0 & \text{if } x \geq 0. \end{cases} \quad (A5)$$

It is easy to see that the response function in Eq. A2 can be simply related to the electron-hole propagator by the relation

$$\chi^0(k, \omega) = -\frac{1}{2\pi k_F} Q_q(u), \quad (A6)$$

where q and u are dimensionless variables defined by

$$\begin{aligned} k &= k_F q \\ \omega &= i k_F q v_F u. \end{aligned} \quad (A7)$$

Therefore, if we rewrite Eq. A1 in terms of the electron-hole propagator and using the dimensionless variables u and q , we obtain

$$\begin{aligned} E_{corr}^{RPA}(r_s) &= \frac{1}{2\pi(\alpha r_s)^2} \int_0^{+\infty} dq \int_0^{+\infty} du q \left\{ \ln \left(1 + \frac{\alpha r_s}{2\pi} v \left(\frac{qb}{\alpha r_s} \right) Q_q(u) \right) - \frac{\alpha r_s}{2\pi} v \left(\frac{qb}{\alpha r_s} \right) Q_q(u) \right\} \\ &= \frac{1}{2\pi(\alpha r_s)^2} \int_0^{+\infty} dq \int_0^{+\infty} du q \sum_{n=2}^{+\infty} \frac{(-1)^{n-1}}{n} \left(\frac{\alpha r_s}{2\pi} \right)^n v^n \left(\frac{qb}{\alpha r_s} \right) Q_q^n(u), \end{aligned} \quad (A8)$$

where $\alpha = 4/\pi$ in 1D. To pass from the first line to the second one we have Taylor expanded the logarithm. Notice that in 1D, in contrast to the 3D and 2D cases,

the integrals converge in *all* orders of the expansion, since $v(qb)$ ($= \tilde{V}_b(q)$ in Eq. 3) diverges only logarithmically at

small q :

$$v(qb) \simeq \begin{cases} -4 \ln(qb) & \text{if } q \rightarrow 0 \\ \frac{2}{q^2 b^2} & \text{if } q \rightarrow +\infty. \end{cases} \quad (\text{A9})$$

Moreover, the leading order in the r_s expansion for Eq. A8 is given by $n = 2$ (i.e. the direct lowest ring diagram in the perturbative expansion of the interaction). Since we are interested in the lowest order r_s expansion of the RPA correlation energy, we keep the term with $n = 2$ and we discard the others. Thus, we get

$$E_{corr}^{RPA} \simeq -\frac{1}{2} \frac{1}{(2\pi)^3} \int_0^{+\infty} dq q v^2 \left(\frac{qb}{\alpha r_s} \right) F(q), \quad (\text{A10})$$

with $F(q) = \int_0^{+\infty} du Q_q^2(u)$ the integral over the dimensionless frequency of the 2-particles electron-hole propagator at a given momentum transfer q . Indeed $F(q)$ can be explicitly written as

$$F(q) = \frac{2\pi}{q} \int_{1-q}^1 dk_1 \int_{1-q}^1 dk_2 \frac{1}{q^2 + q(k_1 + k_2)}, \quad (\text{A11})$$

and for zero q -transfer $F(0) = \pi$. If we rescale the variable q in the integration A10 ($q \rightarrow \frac{\alpha r_s}{b} q$), and we keep the lowest order in r_s , the RPA correlation energy reads:

$$E_{corr}^{RPA} = -\frac{1}{(4\pi)^2} \left(\frac{\alpha r_s}{b} \right)^2 \int_0^{+\infty} dz z v^2(z). \quad (\text{A12})$$

In order to make sure that this is the correct high energy limit of the correlation energy, we need to consider also the second order exchange contribution in the perturbation theory. It is neglected in the RPA approximation, but can yield non trivial corrections in the r_s expansion, like in the two⁵³ and three⁵² dimensional electron gas. The second order exchange is

$$E_{exch}^{II} = \frac{1}{4} \frac{1}{(2\pi)^3} \int_0^{+\infty} dq q v \left(\frac{qb}{\alpha r_s} \right) F_{exch}(q), \quad (\text{A13})$$

where now

$$F_{exch}(q) = \frac{2\pi}{q} \int_{1-q}^1 dk_1 \int_{1-q}^1 dk_2 v \left(\frac{(q + k_1 + k_2)b}{\alpha r_s} \right) \frac{1}{q^2 + q(k_1 + k_2)} \quad (\text{A14})$$

One can easily see that $F_{exch}(0) = \pi v \left(\frac{2b}{\alpha r_s} \right)$. The difference from the second order direct ring (Eqs. A10 and A11) is the vertex interaction $V(q)$ computed at $q+k_1+k_2$ instead of q , and the overall factor is reduced by a factor of 2, due to the spin summation which is now restricted only to the parallel contribution. If we rescale the variable q as before ($q \rightarrow \frac{\alpha r_s}{b} q$), we find

$$\begin{aligned} E_{exch}^{II} &= \frac{1}{2} \frac{1}{(4\pi)^2} \left(\frac{\alpha r_s}{b} \right)^2 \int_0^{+\infty} dz z v(z) v \left(\frac{2b}{\alpha r_s} \right) \\ &= \frac{4A_{exch}}{\pi^6 b^4} r_s^4, \end{aligned} \quad (\text{A15})$$

where we used the asymptotic behavior of the potential $v(x)$ for $x \rightarrow +\infty$ (Eq. A9), and defined $A_{exch} = \int_0^{+\infty} dz z v(z)$. It is apparent that the exchange second order diagram contributes only to the fourth order of r_s . Therefore, at the lowest order in r_s , the correlation energy is:

$$E_{corr} = -\frac{A}{\pi^4 b^2} r_s^2, \quad (\text{A16})$$

with $A = \int_0^{+\infty} dz z v^2(z) = 4.9348$. This result turns out to be the same as a high density extrapolation²² of the correlation energy for the same model studied here, obtained by Gold and Calmels within the so called mean spherical approximation (MSA). In two and three dimensions, the MSA yielded high density expressions of the correlation energy which were slightly different from the RPA findings²³. In this case however, the MSA and the RPA results are in perfect agreement.

APPENDIX B: VARIATIONAL ENERGIES OF CHARGE EXCITATIONS

Let $|\Psi_0\rangle$ be the ground state of the Hamiltonian

$$H = \sum_{k,\sigma} \epsilon(k) c_{k,\sigma}^\dagger c_{k,\sigma} + \frac{1}{2L} \sum_{q \neq 0} V(q) (\rho_{-q} \rho_q - N), \quad (\text{B1})$$

where $\epsilon(k)$ is the dispersion of the non interacting system, $V(q)$ is the Fourier transform of the interaction, and $\rho_q = \sum_{k,\sigma} c_{k+q,\sigma}^\dagger c_{k,\sigma}$ is the Fourier transform of the charge density operator. In analogy with the Feynman construction for the liquid Helium⁵⁴, a variational wave function for a charge excitation (plasmon) with momentum q is given by

$$|\Psi_q\rangle = \rho_q |\Psi_0\rangle. \quad (\text{B2})$$

Its variational energy $\langle \Psi_q | H | \Psi_q \rangle / \langle \Psi_q | \Psi_q \rangle$ is E_q , while the GS energy is E_0 . Notice that the normalization of $|\Psi_q\rangle$ is

$$\langle \Psi_q | \Psi_q \rangle = N S_{\rho\rho}(q) \langle \Psi_0 | \Psi_0 \rangle, \quad (\text{B3})$$

where $S_{\rho\rho}(q) = \frac{1}{N} \langle \rho_{-q} \rho_q \rangle$ is the static charge structure factor. We are now going to find an expression which allows us to estimate the excitation energy of a plasmon with momentum q from knowledge of $S_{\rho\rho}(q)$. We start by evaluating the double commutator

$$[[\rho_q, H], \rho_{-q}] = \sum_k (\epsilon_{k+q} + \epsilon_{k-q} - 2\epsilon_k) c_k^\dagger c_k, \quad (\text{B4})$$

where we used the Hamiltonian in Eq. B1. On the other hand, we have

$$\frac{\langle \Psi_0 | [[\rho_q, H], \rho_{-q}] | \Psi_0 \rangle}{\langle \Psi_0 | \Psi_0 \rangle} = 2N S_{\rho\rho}(q) (E_q - E_0), \quad (\text{B5})$$

by applying the definition of the double commutator $[[\rho_q, H], \rho_{-q}] = \rho_q H \rho_{-q} + \rho_{-q} H \rho_q - \rho_q \rho_{-q} H - H \rho_q \rho_{-q}$. Merging Eq. B4 and Eq. B5, we are led to the following identity:

$$E_q - E_0 = \frac{\langle \Psi_0 | \sum_k (\epsilon_{k+q} + \epsilon_{k-q} - 2\epsilon_k) c_k^\dagger c_k | \Psi_0 \rangle}{2N S_{\rho\rho}(q) \langle \Psi_0 | \Psi_0 \rangle}. \quad (\text{B6})$$

$E_q - E_0$ is an estimate of the plasmon excitation with momentum q . In general the ansatz $|\Psi_q\rangle = \rho_q |\Psi_0\rangle$ is not exact for the lowest energy wave function with momentum q , but gives a variational energy, since it belongs to the same q -subspace as the true excited state and is orthogonal to subspaces with different q' . In the limit of q small, Eq. B6 turns out to be

$$\begin{aligned} E_q - E_0 &\simeq \frac{\langle \Psi_0 | \sum_k \partial_k^2 \epsilon_k c_k^\dagger c_k | \Psi_0 \rangle}{2N \langle \Psi_0 | \Psi_0 \rangle} \frac{q^2}{S_{\rho\rho}(q)} \\ &\simeq \frac{q^2}{S_{\rho\rho}(q)}, \end{aligned} \quad (\text{B7})$$

where we used the quadratic dispersion $\epsilon(k) = k^2$ in Ryd^* units. Therefore, from the knowledge of $S_{\rho\rho}(k)$ calculated for the GS of the system we can evaluate its excitation spectrum in a variational way. Moreover the smaller q is, the better Eq. B7 approximates the true plasmon energy. In the same way, one can estimate the energy of the spin-wave excitations (spinons), by using the relation in Eq. B7 with $S_{\rho\rho}(k)$ replaced by the static spin structure factor $S_{\sigma\sigma}(k)$.

-
- ¹ H. Moritz, Thilo Stöferle, Kenneth Günter, Michael Köhl, and Tilman Esslinger, Phys. Rev. Lett. **94**, 210401 (2005).
² A. Yacoby, H. L. Stormer, N. S. Wingreen, L. N. Pfeiffer, K. W. Baldwin, and K. W. West, Phys. Rev. Lett. **77**, 4612 (1996); Solid State Communications **101**, 77 (1997); L. N. Pfeiffer, A. Yacoby, H. L. Stormer, K. W. Baldwin, J. Hasen, A. Pinczuk, W. Wegscheider, and K. W. West, Microelectron. J. **28**, 817 (1997).
³ S. M. Cronenwett, H. J. Lynch, D. Goldhaber-Gordon, L. P. Kouwenhoven, C. M. Marcus, K. Hirose, N. S. Wingreen, and V. Umansky, Phys. Rev. Lett. **88**, 226805 (2002); D. J. Reilly, T. M. Buehler, J. L. O'Brien, A. R. Hamilton¹, A. S. Dzurak¹, R. G. Clark, B. E. Kane, L. N. Pfeiffer, and K. W. West, Phys. Rev. Lett. **89**, 246801 (2002).
⁴ O. M. Auslaender, H. Steinber, A. Yacoby, Y. Tserkovnyak, B. I. Halperin, K. W. Baldwin, L. N. Pfeiffer, and K. W. West, Science **308**, 88 (2005).
⁵ H. Steinberg, O. M. Auslaender, A. Yacoby, J. Qian, G. A. Fiete, Y. Tserkovnyak, B. I. Halperin, R. de Picciotto, K. W. Baldwin, L. N. Pfeiffer and K. W. West, Phys. Rev. B **73**, 113307 (2006).
⁶ K. Schonhammer and V. Meden, Am J. Phys. **64**, 1168 (1996); J. Voit, Rep. Prog. Phys. **58** 977 (1995).
⁷ O. M. Auslaender, A. Yacoby, R. de Picciotto, K. W. Baldwin, L. N. Pfeiffer, and K. W. West, Science **295**, 825 (2002).
⁸ K. A. Matveev, Phys. Rev. Lett. **92**, 106801 (2004); Phys. Rev. B **70**, 245319 (2004).
⁹ Erich J. Mueller, Phys. Rev. B **72**, 075322 (2005).
¹⁰ Gregory A. Fiete, Jiang Qian, Yaroslav Tserkovnyak, and Bertrand I. Halperin, Phys. Rev. B **72**, 045315 (2005).
¹¹ W. I. Friesen and B. Bergesen, J. Phys. C **13**, 6627 (1980).
¹² A. Gold and A. Ghazali, Phys. Rev. B **41**, 7626 (1990).
¹³ G. Y. Hu and R. F. O'Connell, Phys. Rev. B **42**, 1290 (1990).
¹⁴ G. Y. Hu and S. Das Sarma, Phys. Rev. B **48**, 5469 (1993).
¹⁵ Y. Sun and G. Kirzenow, Phys. Rev. B **47**, 4413 (1993).
¹⁶ H. J. Schulz, Phys. Rev. Lett. **71**, 1864 (1993).
¹⁷ G. Fano and F. Ortolani, A. Parola, L. Ziosi, Phys. Rev. B **60**, 15654 (1999).
¹⁸ B. Valenzuela, S. Fratini, and D. Baeriswyl, Phys. Rev. B **68**, 045112 (2003).
¹⁹ S. Capponi and D. Poilblanc, T. Giamarchi, Phys. Rev. B **61**, 13410 (2000).
²⁰ D. Poilblanc, S. Yunoki, S. Maekawa, and E. Dagotto, Phys. Rev. B **56** R1645 (1997).
²¹ Micheal M. Fogler, Phys. Rev. Lett. **94**, 056405 (2005).
²² L. Calmels, and A. Gold, Phys. Rev. B **56**, 1762 (1997).
²³ A. Gold, and L. Calmels, Solid State Commun. **96**, 101 (1995).
²⁴ L. Camels and A. Gold, Europhys. Lett. **39**, 539 (1997).
²⁵ E. Lieb and D. Mattis, Phys. Rev. **125**, 164 (1962).
²⁶ D. M. Ceperley, J. Stat. Phys. **63**, 1237 (1991).
²⁷ A. Malatesta and G. Senatore, J. Phys. IV **10**, Pr5-341 (2000).
²⁸ C. E. Creffield, W. Häusler, and A. H. MacDonald, Europhys. Lett. **53**, 221 (2001).
²⁹ M. Casula, C. Filippi and S. Sorella, Phys. Rev. Lett. **95**, 100201 (2005).
³⁰ Gao Xianlong, Marco Polini, Reza Asgari, and M. P. Tosi, Phys. Rev. A **73**, 033609 (2006).
³¹ Gao Xianlong, Marco Polini, M. P. Tosi, Vivaldo L. Campo, Jr., and Klaus Capelle, cond-mat/0506570; Gao Xianlong, Marco Polini, M. P. Tosi, Vivaldo L. Campo, Jr., Klaus Capelle, and Marcos Rigol, Phys. Rev. B **73**, 165120 (2006).
³² M. P. Allen, D. J. Tildesley, in *Computer simulation of liquids* (Clarendon, Oxford, 1987)
³³ M. Capello, F. Becca, M. Fabrizio, S. Sorella, and E. Tosatti, Phys. Rev. Lett. **94**, 026406 (2005).
³⁴ Chien-Jung Huang, C. Filippi, and C. J. Umrigar, J. Chem. Phys. **108**, 8838 (1998)
³⁵ T. Gaskell, Proc. Phys. Soc. **77**, 1182 (1961), ibidem **80**, 1091 (1962)
³⁶ R. J. Coldwell, Int. J. Quant. Chem. Symp. **11**, 215 (1977)

- ³⁷ C. J. Umrigar, K. G. Wilson, J. W. Wilkins, Phys. Rev. Lett. **60**, 1719 (1988)
- ³⁸ A. J. Williamson, S. D. Kenny e G. Rajagopal, A. J. James, R. J. Needs, L. M. Fraser and W. M. C. Foulkes, P. Mac-cullum, Phys. Rev. B **53**, 9640 (1996).
- ³⁹ D. F. B. ten Haaf, J. M.J. van Leeuwen, W. van Saarloos, and D. M. Ceperley, Phys. Rev. B **51**, 13039 (1995).
- ⁴⁰ M. Calandra, and S. Sorella, Phys. Rev. B **57**, 11446 (1998).
- ⁴¹ S. Sorella, and L. Capriotti, Phys. Rev. B **61**, 2599 (2000).
- ⁴² C. J. Umrigar, M. P. Nightingale, and K. J. Runge, J. Chem. Phys. **99**, 2865 (1993).
- ⁴³ D. Agosti, F. Pederiva, E. Lipparini, and K. Takayanagi, Phys. Rev. B **57**, 14860 (1998).
- ⁴⁴ J. P. Perdew, and Y. Wang, Phys. Rev. B **45**, 13244 (1992).
- ⁴⁵ C. Attaccalite, S. Moroni, P. Gori-Giorgi, and G. B. Bachelet, Phys. Rev. Lett. **88**, 256601 (2002).
- ⁴⁶ The spin-spin correlation in Eq. 35, computed in Ref. 16, takes into account the leading order term in the large x expansion. Further logarithmic corrections due to the backward scattering (see T. Giamarchi and H. J. Schulz, Phys. Rev. B **39**, 4620 (1989)) can change its prefactor. Correspondingly, also the prefactor for $\exp(-c\sqrt{\log L})$ in the fitting function 38 could be modified, but this change goes beyond the statistical accuracy of our numerical data, the leading and most important term being the constant a_4 in Eq. 38.
- ⁴⁷ M. Casula, and G. Senatore, Chem. Phys. Chem. **6**, 1902 (2005).
- ⁴⁸ L. Reatto, and G. V. Chester, Phys. Rev. **155**, 88 (1967).
- ⁴⁹ M. Fabrizio, A. O. Gogolin, and S. Scheidl, Phys. Rev. Lett. **72**, 2235 (1994).
- ⁵⁰ D. W. Wang, A. J. Millis, and S. Das Sarma, Phys. Rev. B **64**, 193307 (2001).
- ⁵¹ D. Pines, *Elementary excitations in solids* (W. A. Benjamin Inc., New York, 1963).
- ⁵² M. Gell-Mann, and K. A. Brueckner, Phys. Rev. **106**, 364 (1957).
- ⁵³ A. K. Rajagopal, and J. C. kimball, Phys. Rev. B **15**, 2819 (1977).
- ⁵⁴ R. P. Feynman and M. Cohen, Phys. Rev. **102**, 1189 (1956).